Image-Guided Local Delivery Strategies Enhance Therapeutic Nanoparticle Uptake in Solid Tumors

Samdeep K. Mouli,[†] **Patrick Tyler,**[†] **Joseph L. McDevitt,**[†] **Aaron C. Eifler,**[†] **Yang Guo,**[†] **Jodi Nicolai,**[†] **Robert J. Lewandowski,**[†,§] **Weiguo Li,**[†] **Daniel Procissi,**[†] **Robert K. Ryu,**[†,§] **Y. Andrew Wang,**[⊥] **Riad Salem,**[†,§] **Andrew C. Larson,**[†,‡,§] **and Reed A. Omary**[¶,*]

[†]Department of Radiology, Section of Interventional Radiology, Northwestern Memorial Hospital, Robert H. Lurie Comprehensive Cancer Center, Chicago Illinois 60611, United States, [‡]Department of Biomedical Engineering, Northwestern University, Chicago, Illinois 60611, United States, [§]Robert H. Lurie Comprehensive Cancer Center, Northwestern University, Chicago, Illinois 60611, United States, [⊥]Ocean Nanotech, LLC, 700 Research Center Boulevard, Fayetteville, Arkansas 72701, United States, and [¶]Department of Radiology and Radiological Sciences, Vanderbilt University School of Medicine, Nashville, Tennessee 37232, United States

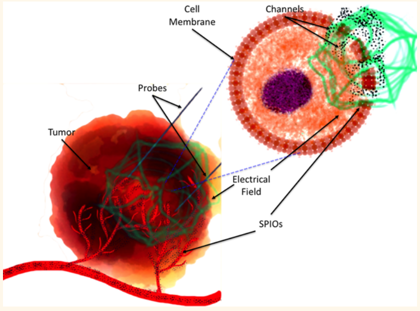

ABSTRACT Nanoparticles (NP) have emerged as a novel class of therapeutic agents that overcome many of the limitations of current cancer chemotherapeutics. However, a major challenge to many current NP platforms is unfavorable biodistribution, and limited tumor uptake, upon systemic delivery. Delivery, therefore, remains a critical barrier to widespread clinical adoption of NP therapeutics. To overcome these limitations, we have adapted the techniques of image-guided local drug delivery to develop nanoablation and nanoembolization. Nanoablation is a tumor ablative strategy that employs image-guided placement of electrodes into tumor tissue to electroporate tumor cells, resulting in a rapid influx of NPs that is not dependent on cellular uptake machinery or stage of the cell cycle. Nanoembolization involves the image-guided delivery of NPs and embolic agents directly into the blood supply of tumors. We describe the design and testing of our innovative local delivery strategies using doxorubicin-functionalized superparamagnetic iron oxide nanoparticles (DOX-SPIOs) in cell culture, and the N1S1 hepatoma and VX2 tumor models, imaged by high resolution 7T MRI. We demonstrate that local delivery techniques result in significantly increased intratumoral DOX-SPIO uptake, with limited off-target delivery in tumor-bearing animal models. The techniques described are versatile enough to be extended to any NP platform, targeting any solid organ malignancy that can be accessed *via* imaging guidance.

KEYWORDS: drug delivery · imaging guidance · magnetic nanoparticles · tumor targeting · cancer therapy · magnetic resonance imaging

Current cancer treatments rely on systemically administered therapies that indiscriminately affect tumor and healthy tissue alike, and therefore are toxic to both tissue types. As such, current therapies are limited by a narrow therapeutic index (ratio of therapeutic to toxic effects) and severe systemic side effects. Nanoparticle (NP) based therapeutics offer an innovative method to overcome the limitations of current agents for several reasons. First, NPs possess unique properties enabling them to serve as simultaneous imaging probes and therapeutic agents, unlike current drugs. Second, they can be tailored to deliver specific drugs[1−3] or target specific molecular mechanisms of cancer.[4−6] The impact of these new agents can only be realized if they are able to reach tumor tissues in sufficient concentrations to exert therapeutic effect.

Conventional intravenous (IV) delivery of most NP platforms results in their sequestration by organs of the reticuloendothelial system (RES), limiting uptake within target tumors, leading to subtherapeutic dosing. Moreover, while all NPs exploit an "enhanced permeability and retention effect" (EPR) for tumor uptake, EPR is still inefficient with relatively low concentrations of NPs reaching tumors.[7] Heterogeneity across tumor types also leads to low and unpredictable rates of NP extravasation.[8] Large tumors, especially metastases, are marked by vascular heterogeneity, reducing perfusion and overall uptake.[9−11] Strategies employing tumor targeting ligands have been met with limited success secondary to tumor heterogeneity

* Address correspondence to reed.omary@vanderbilt.edu.

Received for review May 7, 2013 and accepted August 16, 2013.

10.1021/nn4023119

(no single target) and limited total tumor uptake.[12−16] Long-term efficacy of targeting ligands may also be limited by down-regulation of cell-surface targets over time.[17,18] Several groups have demonstrated that the rate-limiting step for tumor localization is vascular extravasation, which is primarily driven by circulation time.[10,13,19] These barriers have therefore limited the utility and clinical translation of many potential therapeutic agents.

To address issues stemming from unfavorable biodistribution, we have adapted the therapeutic techniques of interventional radiology (IR) to nanoparticle delivery. Interventional radiologists use a wide range of image-guided procedures to treat cancer patients. Real-time imaging guidance and sophisticated navigation techniques are employed for a variety of procedures including tumor ablation, microparticle embolization of vascular tumors, and intra-arterial delivery of chemotherapeutic agents for tumor chemoembolization.[20] These minimally invasive image-guided procedures result in fewer complications, faster recoveries, and reduced costs *versus* traditional therapies.[20] As such, IR may be used to help overcome the limitation of current generation NP platforms with its suite of image-guided techniques. We hypothesized that local, targeted delivery strategies could be exploited for NP-based drug delivery to overcome current unfavorable biodistribution issues. In these proof-of-principle studies, we describe the design, development, and testing of our innovative local delivery strategies.

An essential requirement of this therapeutic approach is a nanoplatform that can be imaged *in vivo* using current generation imaging techniques. To this end, we utilized doxorubicin-functionalized superparamagnetic iron oxide nanoparticles (DOX-SPIO) permitting 7T high-resolution magnetic resonance imaging (MRI). Clinically, SPIO-platforms have been used as MRI contrast agents to stage tumors, plan treatment, and assess response.[21,22] SPIO-based NPs have a long blood retention time, are biodegradable, and have low inherent toxicity.[23,24] They can be functionalized to carry drugs, and their imaging properties can be exploited to monitor drug distribution in target tissue,[24] unlike current drug delivery methods. SPIOs generate tissue contrast *via* a local magnetic field disturbance, causing spin dephasing and signal voids. These susceptibility effects reduce $T2^*$ or equivalently increase $R2^*$ (relaxation rates).[25] These agents can be localized using $R2^*$ parametric maps, with local concentration quantified by measuring proportional changes in $R2^*$.[26] Previous studies have used this linear relationship between concentration and $\Delta R2^*$ to quantify tumor vascularity.[27] $R2^*$ relaxation measurements can estimate the local magnetic dose of SPIOs, and be used as proxy to quantify attached moieties.[28] The use of SPIOs permitted imaging and quantification of therapeutic delivery in our studies.

RESULTS AND DISCUSSION

The 15-nm doxorubicin-functionalized SPIOs were fabricated as previously reported.[29] Briefly, DOX-SPIOs at a concentration of 4 mg/mL were loaded with 0.2 mg doxorubicin per mg iron oxide (IO) (IO MW = 3.7×10^6 g/mol) with 73% loading efficiency (Ocean Nanotech, Springdale, AR). The DOX was coupled to the iron core *via* a pH-labile bond, that permitted selective release within the tumor microenvironment.[29]

Two different delivery strategies were developed, targeting the cellular microenvironment and tumor vasculature at different levels. First we devised nanoablation (Figure 1), a tumor ablative strategy that employs image-guided placement of electrodes into tumor tissue to electroporate tumor cells. Electroporation induces nanoscale defects in the plasma membranes of the cells. This permits rapid influx of extracellular material that is not dependent on cellular uptake machinery or stage of the cell cycle.[30,31] Additionally, electroporation induces transient vascular hypoperfusion within the treated zone,[32] reducing drug washout. The therapeutic effect is further localized to tumors because normal tissue recovers more rapidly.[33−35]

To determine optimal parameters for nanoablation, *in vitro* testing with the N1S1 hepatoma cell line was performed. The goal was to maximize cellular uptake with minimal cellular death. Two million cells/well were plated in 48 well plates. DOX-SPIOs were dissolved in DMEM culture medium and added to individual wells for a final concentration of 50 nM of DOX-SPIOs. Cells were subsequently electroporated using an ECM830 function generator (BTX, Hollinston, MA). The following parameters, based on prior *in vivo* studies,[36,37] were utilized: 8 pulses, 99 μs pulse duration, 1 Hz frequency, 100 ms pulse interval. Voltage was varied from 50 V/cm to 1500 V/cm to determine optimal uptake parameters. All studies were performed in triplicate. Cell viability was determined by flow cytometry, and SPIO uptake was quantified by inductively coupled plasma mass spectrometry (ICP-MS). A dose response curve was subsequently generated demonstrating maximum SPIO uptake with minimal cell death at 500 V/cm (Figure 2).

To determine if this enhanced tumor uptake could be translated *in vivo*, we employed the N1S1 rat model of hepatoma. We hypothesized that localized nanoablation would enhance intratumoral SPIO uptake over surrounding tissues, compared to standard IV delivery. Twenty animals were implanted with N1S1 tumors according to previously published protocols[36,37] and divided into nanoablation and control groups. Dynamic T2* weighted 7T MRI images were obtained before and 24 h after SPIO administration in both groups. DOX-SPIOs (4 mg/mL) suspended in PBS, were injected systemically *via* tail vein at a dose of 0.5 mg/kg in both groups. Nanoablation group animals immediately underwent electroporation using the previously determined settings at 500 V/cm field strength. MRI

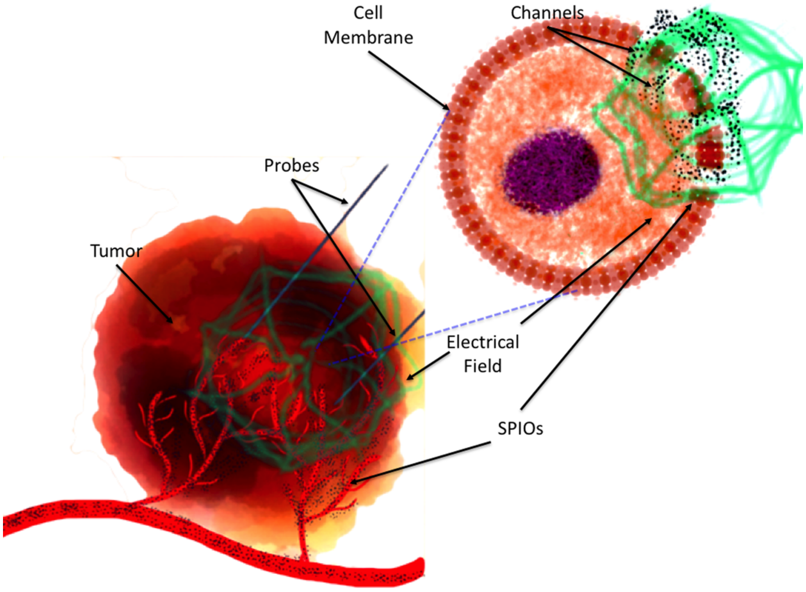

Figure 1. Schematic of nanoablation. Tumor tissue on left, tumor cell on right. Ablation probes are inserted in tumor tissue, generating an electrical field (green). This induces formation of temporary channels in the plasma membrane of the cells of the tumor, permitting rapid SPIO entry.

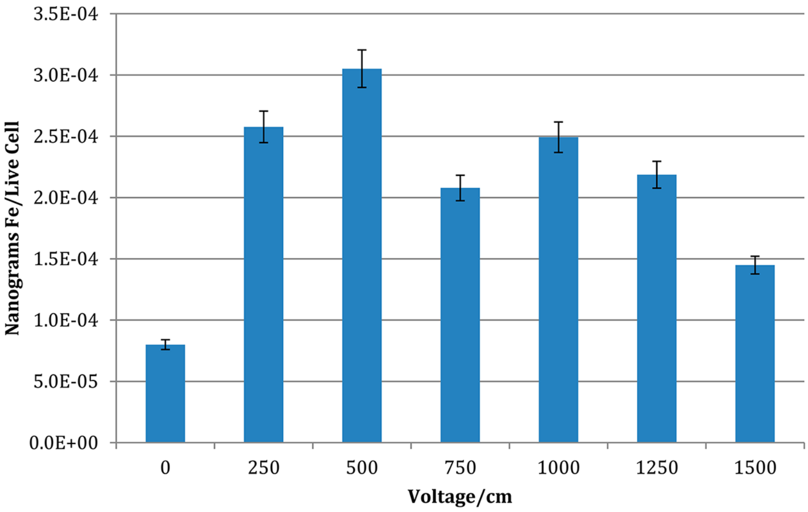

Figure 2. *In vitro* nanoablation testing in the N1S1 cell line. Optimal nanoablation parameters were determined *in vitro*, by varying voltage strength (V/cm), and examining cellular iron (Fe) content *via* ICP-MS, and viability *via* flow cytometry. Optimal uptake was observed at a field strength of 500 V/cm.

$\Delta R2^*$ measurements were applied to quantify intratumoral SPIO uptake noninvasively with $R2^*$ maps produced for tumor tissues across all image slices. Dynamic $T2^*$ weighted images demonstrated dramatically decreased signal intensity within treated tumors, indicative of SPIO uptake (Figures 3 and 4). Minimal signal change was noted in control tumors. Nanoablation resulted in a significant $R2$ signal change in treated animals *versus* controls (103.4 ms *vs* 33.5 ms, $p < 0.05$). To confirm this tumor specific uptake and biodistribution, tumors and organs known to accumulate SPIOs were harvested. SPIO content was quantified with ICP-MS. Nanoablation resulted in significantly higher SPIO uptake within the tumor periphery (27.0 μg/g *vs* 3.5 μg/g, $p < 0.05$) and tumor core (25.3 μg/g vs 6.7 μg/g, $p < 0.05$) compared to IV delivery (Figure 5). Furthermore, nanoablation resulted in significantly less off-target delivery to the healthy liver and spleen ($p < 0.05$).

To further maximize local tumor SPIO uptake and enhance local (tumor-specific) circulation time, we developed nanoembolization. Nanoembolization involves the direct delivery of SPIOs combined with embolic agents, directly into a tumor's blood supply (Figure 6). The goal of embolization is to reduce antegrade blood flow locally to the tumor, thereby increasing the dwell time of the therapeutic agent within the target tumor. Embolization techniques utilizing standard chemotherapeutics or radiopharmaceuticals have been proven to be beneficial in the treatment of primary hepatic and metastatic liver tumors.[38,39] The improved customizability and imaging characteristics of SPIOs may make these agents the ideal next-generation embolic therapy. Furthermore, direct arterial delivery may overcome issues with unfavorable biodistribution and inefficient tumor uptake that limited current therapies prior to arterial-directed delivery.

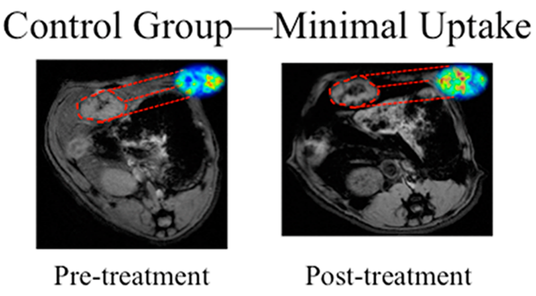

Figure 3. SPIO IV delivery in control N1S1 rats on 7T MRI. Representative axial $T2^*$W GRE images (TE: 11.9 ms) with corresponding $R2^*$ parametric maps from the same animal. Signal intensities were measured in the same plane to determine tumor SPIO uptake. Following SPIO delivery in the control group we saw minimal signal change in the tumor tissue, highlighted here in red, confirming limited uptake with conventional intravenous delivery.

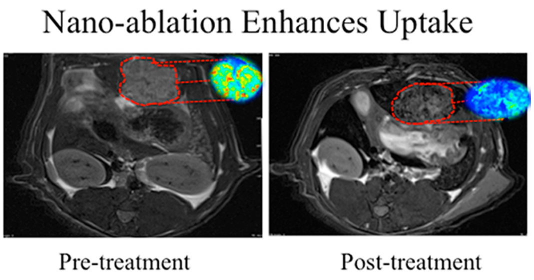

Figure 4. SPIO delivery in nanoablation treated N1S1 rats on 7T MRI. Representative axial $T2^*$W GRE (TE: 11.9 ms) images with corresponding $R2^*$ parametric maps from the same animal. Signal intensities were measured in the same plane to determine tumor SPIO uptake. Following nanoablation, animals in the treatment group demonstrated significant $R2^*$ signal changes within tumor tissues, highlighted in red.

To test this hypothesis *in vivo*, we utilized the VX2 rabbit model of liver cancer (see Materials and Methods).[40−49] This model permitted catheterization of the tumor's arterial supply, and represented an ideal model in which to test local delivery techniques by placing the tumor directly within competing RES tissue. Thirty animals were divided into treatment and control groups. Again, animals in both groups were imaged prior to and after SPIO delivery with 7T $T2^*$ weighted MRI to quantify SPIO uptake. Control animals received DOX-SPIOs suspended in PBS, *via* ear vein injection (0.5 mg/kg). In the nanoembolization group, a microcatheter was selectively advanced into the hepatic artery feeding the tumor under image-guidance. DOX-SPIOs emulsified in lipiodol, the standard chemoembolic agent,[50−52] were delivered intra-arterially (0.5 mg/kg). $\Delta R2^*$ measurements and ICP-MS were used to quantify intratumoral SPIO uptake. Significant increases in $R2^*$ (corresponding to signal reduction in $T2^*$-weighted images) were demonstrated within treated tumors (47.4 ms *vs* 18.9 ms, $p < 0.05$) compared to controls (Figures 7 and 8). This was confirmed pathologically with ICP-MS, which demonstrated a 240% increase in SPIO nanoparticle delivery to the tumor core (188 μg/g *vs* 80 μg/g, $p < 0.05$), and a 260% increase in delivery to the tumor periphery (322 μg/g *vs* 125 μg/g, $p < 0.05$) (Figure 9). Furthermore, nanoembolization resulted in 32% less off-target delivery to healthy liver tissue, and 68% less off-target delivery to the spleen ($p < 0.05$).

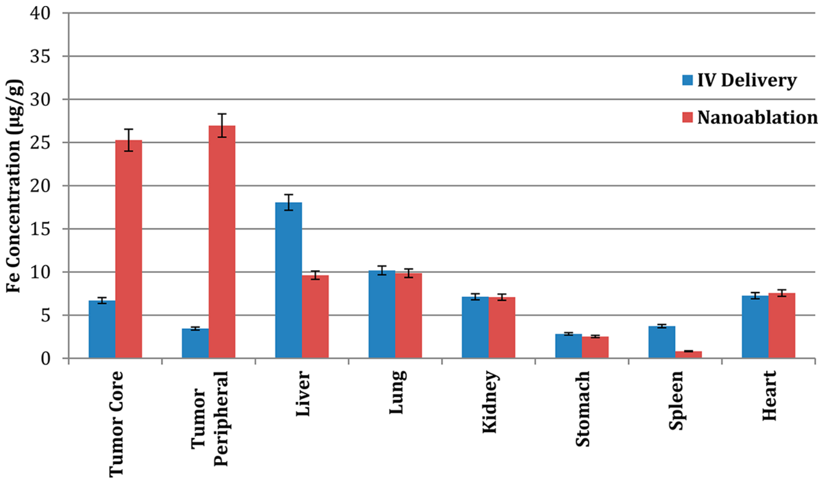

Figure 5. Biodistribution of DOX-SPIOs following administration in N1S1 model. Animals in the nanoablation group demonstrated significantly higher DOX-SPIO uptake within tumor tissue, as well as decreased uptake within healthy liver and spleen tissue, compared to controls ($p < 0.05$).

Several studies have examined the relative contribution of cellular and vascular uptake mechanisms

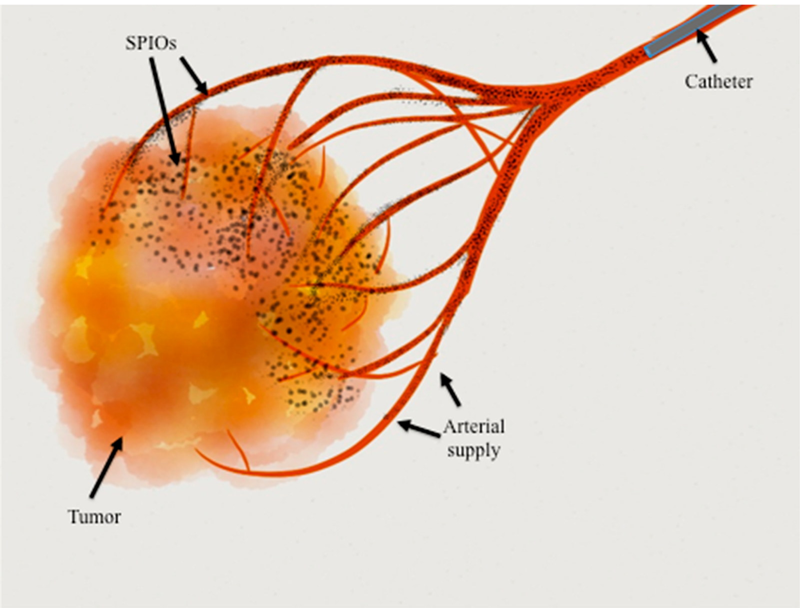

Figure 6. Schematic of nanoembolization: SPIOs along with embolic agents are delivered directly to a tumor's arterial supply *via* an intra-arterial microcatheter. This maximizes intratumoral uptake and minimizes off-target delivery.

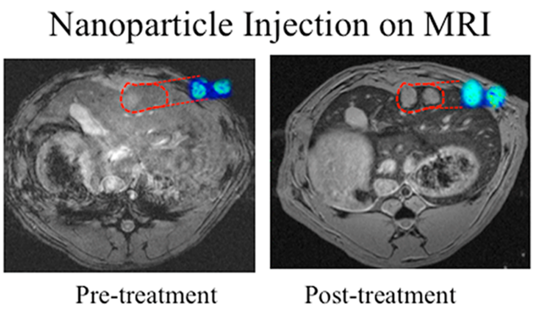

Figure 7. IV SPIO delivery in VX2 rabbit liver cancer model imaged on 7T MRI. Representative axial $T2^*$W GRE (TE: 11.9 ms) images with corresponding $R2^*$ parametric maps from the same animal. Signal intensities were measured in the same plane to determine tumor SPIO uptake. IV delivery did not result in significant $R2^*$ signal changes within tumor tissue, highlighted in red.

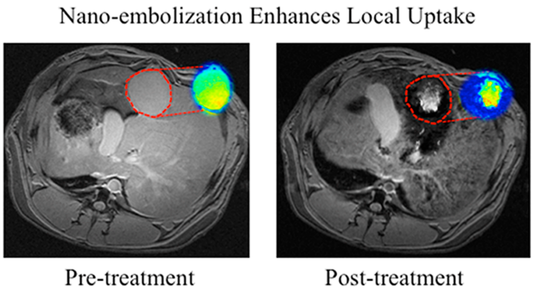

Figure 8. Nanoembolization in VX2 rabbit liver cancer model imaged on 7T MRI. Representative axial $T2^*$W GRE (TE: 11.9 ms) images with corresponding $R2^*$ parametric maps from the same animal. Signal intensities were measured in the same plane to determine tumor SPIO uptake. Nanoembolization resulted in significant $R2^*$ signal changes within tumor tissue, highlighted in red.

in tumor therapy.[10−12,53] As nanoablation and nanoembolization enhance intratumoral SPIO uptake *via* different mechanisms (cellular *vs* vascular), we hypothesized that their effects could be additive. A combination approach may promote synergy between these distinct physiologic pathways.

To determine the optimal temporal window to permit maximal SPIO uptake, delivery-time dependent uptake profiles were determined *in vivo*. Using a VX2 tumor rabbit hindlimb model (see Materials and Methods), eight tumors were implanted. Again, a microcatheter was selectively advanced into the artery feeding the tumor, and SPIOs (0.5 mg/kg), emulsified in lipiodol, were delivered. Electroporation was performed at progressive time points ranging from 3 min before to 3 min after intra-arterial delivery. ICP-MS and $T2^*$-weighted MR imaging both demonstrated that intratumoral SPIO concentrations were significantly increased (2.9 fold, $p < 0.05$) when electroporation was performed 1.5 to 2 min following intra-arterial delivery.

Next, using the VX2 liver cancer model, the synergistic effects of nanoablation and nanoembolization were studied. Ten animals were implanted with hepatic VX2 tumors, as previously described.[40−49] Again, a microcatheter was selectively advanced into the hepatic artery feeding the tumor under image-guidance. DOX-SPIOs emulsified in lipiodol, were delivered, followed by nanoablation 1.5 min later. Animals were imaged *via* 7T $T2^*$-weighted MRI pre- and post-treatment to quantify $\Delta R2^*$. Tumor and healthy liver tissue were harvested for SPIO quantification *via* ICP-MS. Combination therapy (Figures 10 and 11) resulted in significantly increased SPIO uptake over nanoembolization alone in both the tumor core (901 μg/g *vs* 188 μg/g, $p < 0.05$), and tumor periphery (1623 μg/g *vs* 321 μg/g, $p < 0.05$). Furthermore, no

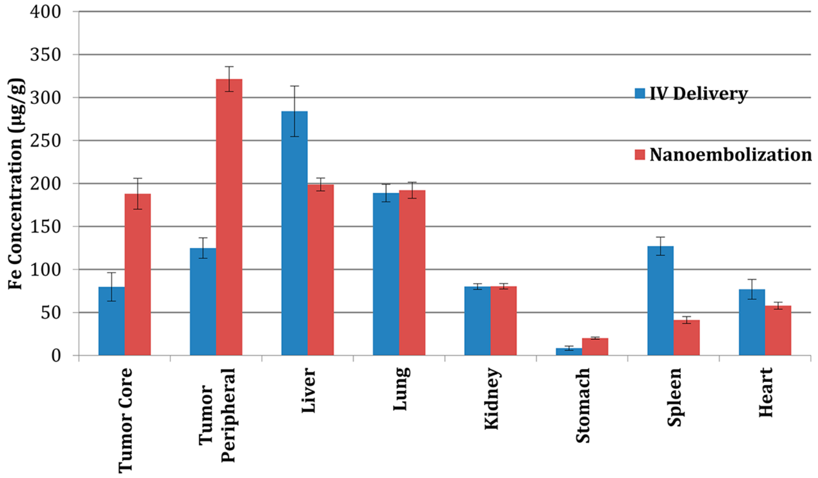

Figure 9. Biodistribution of DOX-SPIOs following administration in VX2 rabbit model. Animals in the nanoembolization group demonstrated significantly higher DOX-SPIO uptake within tumor tissue, as well as decreased uptake within healthy liver and spleen tissue, compared to controls ($p < 0.05$).

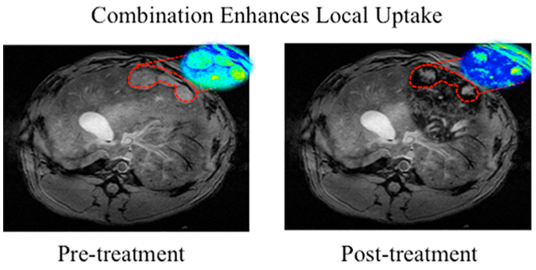

Figure 10. Combination nanoablation and nanoembolization in VX2 rabbit model on 7T MRI. Representative axial $T2^*$W GRE images (TE: 11.9 ms) with corresponding $R2^*$ parametric maps from the same animal. Signal intensities were measured in the same plane to determine tumor SPIO uptake. Combination therapy resulted in significant signal change within tumor tissue, as depicted here in red.

significant difference in delivery to healthy liver tissue was observed ($p = 0.67$). These results demonstrated the significant impact of our proposed combination approach (nanoablation + nanoembolization) for tumor targeted SPIO nanoparticle delivery.

CONCLUSION

Optimization of drug delivery is a central issue in oncology. There is great potential for image-guided strategies to enhance NP delivery, overcoming the barriers related to nontarget uptake by the RES, tumor perfusion, and tissue heterogeneity. To maximize the therapeutic index of novel nanotherapies, it is critical to preferentially deliver these agents to target tissues rather than healthy normal tissue. We have

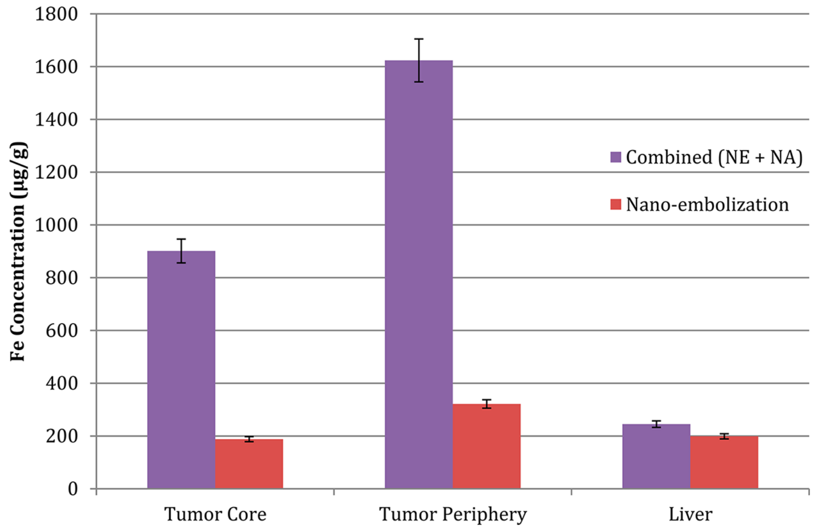

Figure 11. Biodistribution of DOX-SPIOs in tumor and liver tissue following combination therapy (nanoembolization followed by nanoablation) in VX2 rabbit model. Combination therapy resulted in significantly increased delivery to both the tumor core and periphery, compared to nanoembolization alone ($p < 0.05$). Furthermore, a significant difference in off-target delivery, to healthy liver tissue, was not observed (p = ns).

demonstrated that this control can be achieved by adopting image-guided ablative and intra-arterial techniques for the delivery of NPs. By applying these local delivery techniques, we have demonstrated enhanced intratumoral SPIO uptake in contrast to standard IV delivery strategies. Furthermore, these strategies limit nonspecific delivery to the RES. The effectiveness of these techniques does not rely on sophisticated targeting mechanisms or cellular uptake machinery. Critically, these benefits do not depend on the composition or specific characteristics of the NP delivered. As such, these techniques are versatile enough to be extended to any NP platform, targeting any solid organ malignancy that can be accessed *via* image-guidance. Future longitudinal studies will focus on further validating the therapeutic efficacy of these techniques.

MATERIALS AND METHODS

Doxorubicin Superparamagnetic Iron-Oxide Nanoparticles. SPIOs were prepared using iron oxide micropowder as the iron precursor, oleic acid as the ligands, and octadecene as the solvent as described.[54] The core size and hydrodynamic size of the SPIOs were measured using transmission electron microscopy (TEM), and light scattering scan, respectively. We used IO nanoparticles with 10 nm core size for this study. The particles were coated with amphiphilic polymers reported previously,[55] which stabilizes SPIOs in water and provides reactive carboxyl groups on the particle surface for bioconjugation. To reduce nonspecific binding and uptake by cells, PEG−diamine (molecular weight of 2000) was conjugated to SPIOs by ethyl-3-dimethyl amino propyl carbodiimide (EDAC) coupling method.

Doxorubicin HCl in 0.15 M NaCl at 0.5 mg/mL was added to 10 nm iron oxide nanoparticles and vortex for 1 h at room temperature. The free DOX molecules were separated from the encapsulated DOX-SPIOs by magnetic separator (SuperMag Separator, Ocean NanoTech, Springdale AR). The DOX loading amount was about 20% (w/w(Fe)) calculated by free DOX left from the supernatant.

Cell Line and Culture. The N1−S1 rat hepatoma cell line (ATCC, Manassas, VA) was obtained and cultured in Dulbecco's Modified Eagle's Medium (DMEM) (ATCC, Manassas, VA) supplemented with 10% fetal bovine serum (Sigma-Aldrich, St. Louis, MO) and 1% penicillin streptomycin (Invitrogen, Carlsbad, CA). Cells were maintained in suspension culture flasks at 37 °C in a humidified atmosphere containing 5% CO_2. Trypan blue staining was performed before each tumor implantation procedure to verify >90% cell viability.

Flow Cytometry and Fluorescence Microscopy. Cells were harvested and suspended in cold PBS with 2% bovine serum albumin at a concentration of 50000 cells/mL, incubated with propidium iodide for 30 min at room temperature (RT), washed three times with cold PBS, and centrifuged at 1250 rpm for 5 min. Afterward, the cells were washed and analyzed using a Beckman Coulter Moflo Cell Sorter, which is equipped with five lasers, with excitation lines ranging from 350 nm to 647 nm (Beckman Coulter, Brea, CA).

Animal Models. *N1S1 Cells and Rat Model.* All experiments were approved by an Institutional Animal Care and Use Committee. Twenty male Sprague−Dawley rats (Charles River, Wilmington, MA) weighing 250−380 g were used for the experiments, all of which received a standard laboratory diet with free access to water.

Tumor inoculation was performed according to a previously published procedure.[56] Subjects were anesthetized with a hind limb injection of 100 mg/kg ketamine (Ketaset, Fort Dodge Animal Health, Fort Dodge, IA) and 4 mg/kg xylazine (Isothesia; Abbot Laboratories, North Chicago, IL). The left lateral lobe of the liver was exposed *via* mini-laparotomy and externalized using cotton-tipped applicators. Using a sterile insulin syringe, 5 million cells of N1−S1 suspended in 0.2 mL of DMEM were injected into the left lateral lobe of the liver. The incision was then closed using a double-layer suture technique and a 0.75 × 0.75 cm square of Surgicel hemostat (Ethicon, Somerville, NJ) was placed over the incision. Buprenorphine (2 mg/kg) and meloxicam (2 mg/kg) were administered twice daily for 48 h after surgery, and animals were monitored for postsurgical recovery until wound healing was complete.

VX2 Rabbit. Our institutional Animal Care and Use Committee approved all experiments. Forty-five New Zealand white rabbits weighing 4−5 kg were used in these experiments. The VX2 tumor model was used because the VX2 tumor blood supply is almost entirely from the hepatic artery, and rabbit hepatic arteries are sufficiently large to permit catheterization.[57] VX2 cells were initially grown in the hind limb of five donor rabbits. Tumor specimens approximately 2 mm in diameter were harvested and implanted in the left lobe of the liver in the 40 remaining rabbits *via* mini-laparotomy. Tumors were allowed to grow for 3−4 weeks before imaging. During imaging procedures, rabbits were anesthetized with intramuscularly administered ketamine (Ketaset; Fort Dodge Animal Health, Fort Dodge, IA), and xylazine (AnaSed Injection; Lloyd Laboratories, Shenandoah, IA), followed by inhaled isoflurane (Isothesia; Abbott Laboratories, North Chicago, IL).

Magnetic Resonance Imaging and Analysis. A Bruker 7T ClinScan MRI horizontal bore scanner (Bruker, Billerica, MA) was employed for all rodent scans. A mixture of 2−5% isofluorane and 2L/min oxygen were supplied *via* facemask to the subjects throughout imaging. A small animal monitoring system (SA Instruments, Stony Brook, NY) was used to ensure appropriate sedation and monitor physiologic parameters at all times. Localizer and $T2$-weighted anatomical scans were performed to verify animal positioning and tumor presence. $T2^*$ measurements were obtained before and after treatment using the following scan parameters: $T2^*/R2^*$ measurements were obtained by using a multiple-gradient-echo (mGRE) sequence with TR/TEs = 200/2.6, 5.7, 8.8, 11.9 ms; 30° flip angle, 1-mm section thickness, 65-mm field of view, 192 × 192 matrix, readout bandwidth of 360 Hz/pixel.

Our quantitative $T2^*/R2^*$ measurements were fit to monoexponential equations voxelwise to extract $T2^*/R2^*$ maps using Matlab 7.1 (MathWorks, Natick, MA). A specific region of interest (ROI) was drawn in each $R2$ or $R2^*$ map, then averaged over the ROI to generate a mean $R2$ or $R2^*$ value.

Treatment. *Rodent Studies.* MRI was performed 7−10 days after tumor implantation to confirm tumor growth, and tumor size was quantified by measuring maximum diameter, in accordance with Response Evaluation Criteria in Solid Tumors (RECIST) guidelines.[58] After removal from the MRI scanner, nanoablation (NA) was performed as follows: A mini-laparotomy exposed the liver, and cotton-tipped applicators were employed to externalize the left lateral lobe of the liver and place it on a sheet of gauze. DOX-SPIOs suspended in PBS (0.5 mg/kg) were then injected into the tail vein. Two minutes after DOX-SPIO injection, electroporation was applied *via* a two-pronged electroporation tool (BTX, Holliston, MA) with two 0.4 mm-diameter needles separated by 1 cm. Eight 500 V pulses of 100 μs each with 100 ms between pulses were delivered with an ECM830 function generator (BTX, Holliston, MA) in accordance with previous electroporation optimization studies.[59] The liver was then returned to the abdominal cavity, and the incision was closed *via* suture. Twenty-four hours following nanoablation, the subjects were returned to MRI for post-treatment imaging. For IV control animals, DOX-SPIOs suspended in PBS were delivered *via* tail vein (0.5 mg/kg). Twenty-four hours following delivery animals underwent MR imaging. Subsequently, the subjects in both groups were euthanized using pentobarbital (Euthasol , Virbac Animal Health, Fort Worth, TX) for tissue harvest.

Rabbit Studies. Each rabbit was catheterized with X-ray fluoroscopic guidance by using a C-arm unit (PowerMobil; Siemens Medical Solutions, Erlangen, Germany). Vascular access was achieved in the femoral artery through surgical cutdown. A 3-F vascular sheath was first placed, and a 2-F catheter was then inserted within this sheath. The 2-F catheter (JB-1; Cook, Bloomington, ID) was advanced over a 0.014-in.-diameter guidewire into the targeted arteries. Conventional digital subtraction angiographic procedures were performed by an attending interventional radiologist (R.A.O., with greater than 15 years of experience). A 4:1 DOX-SPIO:lipiodol embolic emulsion was delivered *via* arterial catheter. Lipiodol is used clinically in standard chemoembolization protocols as an emulsifier to deliver drugs. It also has an embolic effect, thereby promoting dwell time of therapeutics within the targeted tumor. For animals undergoing combination treatment, electroporation was then performed *via* our previously described protocol above. The animals were then transferred to an MR imaging unit.

Necropsy and Tissue Analysis. Tissue iron concentration was determined *via* inductively coupled plasma mass-spectrometry (ICP-MS) and used as proxy for SPIO uptake and Doxorubicin concentration. Necropsy was performed and the tumor was separated from the surrounding hepatic parenchyma. Prior studies in both the VX2 rabbit and N1S1 rat models[49,57,60−62] have demonstrated a histologic difference between the tumor core and periphery, with highly vascularized tissue found in the tumor periphery, and poorly vascularized tissue in the tumor core. To account for these differences, after necropsy, using surgical microdissection, the central tumor was extracted and the viable margin of each tumor was sectioned into 4 quadrants, according to previously published protocols.[60] Specimens were sectioned if necessary such that each sample was less than 0.1 g and were placed in an Eppendorf tube (Eppendorf International, Hamburg, Germany). The samples were dissolved in 800 μL of trace metal grade nitric acid (70%). Digested samples were filtered with 0.45 μm PTFE syringe filters, then 20 μL of digested sample was transferred to a 15 mL metal-free tube and diluted with 12 mL of laboratory grade water to 2−3% acid. Calibration standards of 0.5, 1, 5, 10, 20, 50, and 100 ppb Fe in 2% nitric acid buffer were prepared, as well as a blank solution. An yttrium internal standard was added to both standards and samples, and ICP-MS was performed on a Thermo XSeries II ICP-MS (Thermo-Fisher, Waltham, MA). This returned a concentration of iron in parts per billion, which was converted to micrograms of iron. From the weight of the tissue, and volume of the digested homogenate, iron levels were normalized to amount per gram of wet tissue. Tissues from animals receiving sham procedures (saline injection) were used as controls for endogenous iron content. The Fe content in each organ was subtracted by the corresponding averaged value from sham animals according to previously published protocols.[24,63]

Statistical Analysis. Data are expressed as means ± standard deviation from a minimum of three samples, unless otherwise indicated. Statistical analyses were carried out using a statistics software program (SPSS Statistics, IBM, Armonk, NY). For multiple comparisons, a one-way analysis of variance (ANOVA) with post-test (Kruskal−Wallis test with post-test) was used; $p < 0.05$ was considered to indicate a statistically significant difference.

Conflict of Interest: The authors declare no competing financial interest.

Acknowledgment. This work was supported by Robert H. Lurie Comprehensive Cancer Center, and the National Cancer Institute Grants R01CA159178, and R01CA141047.

REFERENCES AND NOTES

1. Jain, T. K.; Morales, M. A.; Sahoo, S. K.; Leslie-Pelecky, D. L.; Labhasetwar, V. Iron Oxide Nanoparticles for Sustained Delivery of Anticancer Agents. *Mol. Pharm.* **2005**, *2*, 194–205.
2. Sun, C.; Lee, J. S. H.; Zhang, M. Magnetic Nanoparticles in MR Imaging and Drug Delivery. *Adv. Drug Delivery Rev.* **2008**, *60*, 1252–1265.
3. Kettering, M.; Zorn, H.; Bremer-Streck, S.; Oehring, H.; Zeisberger, M.; Bergemann, C.; Hergt, R.; Halbhuber, K. J.; Kaiser, W. A.; Hilger, I. Characterization of Iron Oxide Nanoparticles Adsorbed with Cisplatin for Biomedical Applications. *Phys, Med, Biol.* **2009**, *54*, 5109–5121.
4. Peng, X-H; Qian, X.; Mao, H.; Wang, A. Y.; Chen, Z. G.; Nie, S.; Shin, D. M. Targeted Magnetic Iron Oxide Nanoparticles for Tumor Imaging and Therapy. *Int. J. Nanomed.* **2008**, *3*, 311–321.
5. Yang, L.; Mao, H.; Cao, Z.; Wang, Y. A.; Peng, X.; Wang, X.; Sajja, H. K.; Wang, L.; Duan, H.; Ni, C.; *et al.* Molecular Imaging of Pancreatic Cancer in an Animal Model Using Targeted Multifunctional Nanoparticles. *Gastroenterology* **2009**, *136*, 1514–1525 e1512.
6. Davis, M. E.; Chen, Z. G.; Shin, D. M. Nanoparticle Therapeutics: An Emerging Treatment Modality for Cancer. *Nat. Rev. Drug Discovery* **2008**, *7*, 771–782.
7. Jain, R. K.; Stylianopoulos, T. Delivering Nanomedicine to Solid Tumors. *Nat. Rev. Clin. Oncol.* **2010**, *7*, 653–664.
8. de la Zerda, A.; Bodapati, S.; Teed, R.; May, S. Y.; Tabakman, S. M.; Liu, Z.; Khuri-Yakub, B. T.; Chen, X.; Dai, H.; Gambhir, S. S. Family of Enhanced Photoacoustic Imaging Agents for High-Sensitivity and Multiplexing Studies in Living Mice. *ACS Nano* **2012**, *6*, 4694–4701.
9. Fang, J.; Nakamura, H.; Maeda, H. The EPR Effect: Unique Features of Tumor Blood Vessels for Drug Delivery, Factors Involved, and Limitations and Augmentation of the Effect. *Adv. Drug Delivery Rev.* **2010**, 10.1016/j.addr.2010.04.009.
10. Minchinton, A. I.; Tannock, I. F. Drug Penetration in Solid Tumours. *Nat. Rev. Cancer* **2006**, *6*, 583–592.
11. Dreher, M. R.; Liu, W.; Michelich, C. R.; Dewhirst, M. W.; Yuan, F.; Chilkoti, A. Tumor Vascular Permeability, Accumulation, and Penetration of Macromolecular Drug Carriers. *J. Natl. Cancer Inst.* **2006**, *98*, 335–344.
12. Danquah, M. K.; Zhang, X. A.; Mahato, R. I. Extravasation of Polymeric Nanomedicines across Tumor Vasculature. *Adv. Drug Delivery Rev.* **2010**, 10.1016/j.addr.2010.11.005.
13. Huang, X.; Peng, X.; Wang, Y.; Wang, Y.; Shin, D. M.; El-Sayed, M. A.; Nie, S. A Reexamination of Active and Passive Tumor Targeting by Using Rod-Shaped Gold Nanocrystals and Covalently Conjugated Peptide Ligands. *ACS Nano* **2010**, *4*, 5887–5896.
14. Nie, S. Understanding and Overcoming Major Barriers in Cancer Nanomedicine. *Nanomedicine (London).* **2010**, *5*, 523–528.
15. Bartlett, D. W.; Su, H.; Hildebrandt, I. J.; Weber, W. A.; Davis, M. E. Impact of Tumor-Specific Targeting on the Biodistribution and Efficacy of Sirna Nanoparticles Measured by Multimodality *in Vivo* Imaging. *Proc. Natl. Acad. Sci. U.S.A.* **2007**, *104*, 15549–15554.
16. Kirpotin, D. B.; Drummond, D. C.; Shao, Y.; Shalaby, M. R.; Hong, K.; Nielsen, U. B.; Marks, J. D.; Benz, C. C.; Park, J. W. Antibody Targeting of Long-Circulating Lipidic Nanoparticles Does Not Increase Tumor Localization but Does Increase Internalization in Animal Models. *Cancer Res.* **2006**, *66*, 6732–6740.
17. Valastyan, S.; Weinberg, R. A. Tumor Metastasis: Molecular Insights and Evolving Paradigms. *Cell* **2011**, *147*, 275–292.
18. Zhou, B. B.; Zhang, H.; Damelin, M.; Geles, K. G.; Grindley, J. C.; Dirks, P. B. Tumour-Initiating Cells: Challenges and Opportunities for Anticancer Drug Discovery. *Nat. Rev. Drug Discovery* **2009t**, *8*, 806–823.
19. Dreher, M. R.; Liu, W.; Michelich, C. R.; Dewhirst, M. W.; Yuan, F.; Chilkoti, A. Tumor Vascular Permeability, Accumulation, and Penetration of Macromolecular Drug Carriers. *J. Natl. Cancer Inst.* **2006**, *98*, 335–344.
20. Solomon, S. B.; Silverman, S. G. Imaging in Interventional Oncology. *Radiology* **2010**, *257*, 624–640.
21. Weber, M. A.; Giesel, F. L.; Stieltjes, B. MRI for Identification of Progression in Brain Tumors: From Morphology to Function. *Expert Rev. Neurother.* **2008**, *8*, 1507–1525.
22. Khoo, V. S.; Joon, D. L. New Developments in MRI for Target Volume Delineation in Radiotherapy. *Br. J. Radiol.* **2006**, *79* (Spec No 1), S2−15.

23. Levy, M.; Luciani, N.; Alloyeau, D.; Elgrabli, D.; Deveaux, V.; Pechoux, C.; Chat, S.; Wang, G.; Vats, N.; Gendron, F.; et al. Long Term *in Vivo* Biotransformation of Iron Oxide Nanoparticles. *Biomaterials* **2011**, *32*, 3988–3999.
24. Jain, T. K.; Reddy, M. K.; Morales, M. A.; Leslie-Pelecky, D. L.; Labhasetwar, V. Biodistribution, Clearance, and Biocompatibility of Iron Oxide Magnetic Nanoparticles in Rats. *Mol. Pharm.* **2008**, *5*, 316–327.
25. Winkelmann, S.; Schaeffter, T.; Weiss, S.; Eggers, H.; Doessel, O. Simultaneous Imaging and *R*2* Mapping Using a Radial Multi-Gradient-Echo (Rmge) Sequence. *J. Magn. Reson. Imaging* **2006**, *24*, 939–944.
26. Yablonskiy, D. A.; Haacke, E. M. Theory of NMR Signal Behavior in Magnetically Inhomogeneous Tissues: The Static Dephasing Regime. *Magn. Reson. Med.* **1994**, *32*, 749–763.
27. Bremer, C.; Mustafa, M.; Bogdanov, A., Jr.; Ntziachristos, V.; Petrovsky, A.; Weissleder, R. Steady-State Blood Volume Measurements in Experimental Tumors with Different Angiogenic Burdens a Study in Mice. *Radiology* **2003**, *226*, 214–220.
28. Bowen, C. V.; Zhang, X.; Saab, G.; Gareau, P. J.; Rutt, B. K. Application of the Static Dephasing Regime Theory to Superparamagnetic Iron-Oxide Loaded Cells. *Magn. Reson. Med.* **2002**, *48*, 52–61.
29. Yang, L.; Cao, Z.; Sajja, hK; Mao, H.; Wang, L.; Geng, H.; Xu, H.; Jiang, T.; Wood, W. C.; Nie, S.; *et al*. Development of Receptor Targeted Magnetic Iron Oxide Nanoparticles for Efficient Drug Delivery and Tumor Imaging. *J. Biomed. Nanotechnol.* **2008**, *4*, 439–449.
30. Hui, S. W. Overview of Drug Delivery and Alternative Methods to Electroporation. *Methods Mol. Biol.* **2008**, *423*, 91–107.
31. Walczak, P.; Kedziorek, D. A.; Gilad, A. A.; Lin, S.; Bulte, J. W. Instant MR Labeling of Stem Cells Using Magnetoelectroporation. *Magn. Reson. Med.* **2005**, *54*, 769–774.
32. Mir, L. M.; Orlowski, S. The Basis of Electrochemotherapy. *Methods Mol. Med.* **2000**, *37*, 99–117.
33. Tounekti, O.; Pron, G.; Belehradek, J., Jr.; Mir, L. M. Bleomycin, an Apoptosis-Mimetic Drug That Induces Two Types of Cell Death Depending on the Number of Molecules Internalized. *Cancer Res.* **1993**, *53*, 5462–5469.
34. Tounekti, O.; Belehradek, J., Jr.; Mir, L. M. Relationships between DNA Fragmentation, Chromatin Condensation, and Changes in Flow Cytometry Profiles Detected During Apoptosis. *Exp. Cell Res.* **1995**, *217*, 506–516.
35. Mitchell, M. S. Combining Chemotherapy with Biological Response Modifiers in Treatment of Cancer. *J. Natl. Cancer Inst.* **1988**, *80*, 1445–1450.
36. Guo, Y.; Zhang, Y.; Klein, R.; Nijm, G. M.; Sahakian, A. V.; Omary, R. A.; Yang, G-Y; Larson, A. C. Irreversible Electroporation Therapy in the Liver: Longitudinal Efficacy Studies in a Rat Model of Hepatocellular Carcinoma. *Cancer Res.* **2010**, *70*, 1555–1563.
37. Zhang, Y.; Guo, Y.; Ragin, A. B.; Lewandowski, R. J.; Yang, G-Y; Nijm, G. M.; Sahakian, A. V.; Omary, R. A.; Larson, A. C. MR Imaging to Assess Immediate Response to Irreversible Electroporation for Targeted Ablation of Liver Tissues: Preclinical Feasibility Studies in a Rodent Model. *Radiology* **2010**, *256*, 424–432.
38. Coldwell, D.; Sangro, B.; Salem, R.; Wasan, H.; Kennedy, A. Radioembolization in the Treatment of Unresectable Liver Tumors: Experience across a Range of Primary Cancers. *Am. J. Clin. Oncol.* **2012**, *35*, 167–177.
39. Lewandowski, R. J.; Kulik, L. M.; Riaz, A.; Senthilnathan, S.; Mulcahy, M. F.; Ryu, R. K.; Ibrahim, S. M.; Sato, K. T.; Baker, T.; Miller, F. H.; *et al*. A Comparative Analysis of Transarterial Downstaging for Hepatocellular Carcinoma: Chemoembolization *versus* Radioembolization. *Am. J. Transplant.* **2009**, *9*, 1920–1928.
40. Virmani, S.; Rhee, T. K.; Ryu, R. K.; Sato, K. T.; Lewandowski, R. J.; Mulcahy, M. F.; Kulik, L. M.; Szolc-Kowalska, B.; Woloschak, G. E.; Yang, G. Y.; *et al*. Comparison of Hypoxia-Inducible Factor-1alpha Expression before and after Transcatheter Arterial Embolization in Rabbit Vx2 Liver Tumors. *J. Vasc. Interventional Radiol.* **2008**, *19*, 1483–1489.
41. Gupta, T.; Virmani, S.; Neidt, T. M.; Szolc-Kowalska, B.; Sato, K. T.; Ryu, R. K.; Lewandowski, R. J.; Gates, V. L.; Woloschak, G. E.; Salem, R.; et al. MR Tracking of Iron-Labeled Glass Radioembolization Microspheres During Transcatheter Delivery to Rabbit Vx2 Liver Tumors: Feasibility Study. *Radiology* **2008**, *249*, 845–854.
42. Wang, D.; Virmani, S.; Tang, R.; Szolc-Kowalska, B.; Woloschak, G.; Omary, R. A.; Larson, A. C. Four-Dimensional Transcatheter Intraarterial Perfusion (Trip)-MRI for Monitoring Liver Tumor Embolization in Vx2 Rabbits. *Magn. Reson. Med.* **2008**, *60*, 970–975.
43. Virmani, S.; Harris, K. R.; Szolc-Kowalska, B.; Paunesku, T.; Woloschak, G. E.; Lee, F. T.; Lewandowski, R. J.; Sato, K. T.; Ryu, R. K.; Salem, R.; *et al*. Comparison of Two Different Methods for Inoculating Vx2 Tumors in Rabbit Livers and Hind Limbs. *J. Vasc. Interventional Radiol.* **2008**, *19*, 931–936.
44. Deng, J.; Virmani, S.; Young, J.; Harris, K.; Yang, G. Y.; Rademaker, A.; Woloschak, G.; Omary, R. A.; Larson, A. C. Diffusion-Weighted Propeller MRI for Quantitative Assessment of Liver Tumor Necrotic Fraction and Viable Tumor Volume in Vx2 Rabbits. *J. Magn. Reson. Imaging* **2008**, *27*, 1069–1076.
45. Wang, D.; Bangash, A. K.; Rhee, T. K.; Woloschak, G. E.; Paunesku, T.; Salem, R.; Omary, R. A.; Larson, A. C. Liver Tumors: Monitoring Embolization in Rabbits with Vx2 Tumors—Transcatheter Intraarterial First-Pass Perfusion MR Imaging. *Radiology* **2007**, *245*, 130–139.
46. Rhee, T. K.; Young, J. Y.; Larson, A. C.; Haines, G. K., 3rd; Sato, K. T.; Salem, R.; Mulcahy, M. F.; Kulik, L. M.; Paunesku, T.; Woloschak, G. E.; *et al*. Effect of Transcatheter Arterial Embolization on Levels of Hypoxia-Inducible Factor-1alpha in Rabbit Vx2 Liver Tumors. *J. Vasc. Interventional Radiol.* **2007**, *18*, 639–645.
47. Rhee, T. K.; Ryu, R. K.; Bangash, A. K.; Wang, D.; Szolc-Kowalska, B.; Harris, K. R.; Sato, K. T.; Chrisman, H. B.; Vogelzang, R. L.; Paunesku, T.; *et al*. Rabbit Vx2 Tumors as an Animal Model of Uterine Fibroids and for Uterine Artery Embolization. *J. Vasc. Interventional Radiol.* **2007**, *18*, 411–418.
48. Larson, A. C.; Rhee, T. K.; Deng, J.; Wang, D.; Sato, K. T.; Salem, R.; Paunesku, T.; Woloschak, G.; Mulcahy, M. F.; Li, D.; *et al*. Comparison between Intravenous and Intraarterial Contrast Injections for Dynamic 3d MRI of Liver Tumors in the Vx2 Rabbit Model. *J. Magn. Reson. Imaging* **2006**, *24*, 242–247.
49. Deng, J.; Rhee, T. K.; Sato, K. T.; Salem, R.; Haines, K.; Paunesku, T.; Mulcahy, M. F.; Miller, F. H.; Omary, R. A.; Larson, A. C. *In Vivo* Diffusion-Weighted Imaging of Liver Tumor Necrosis in the Vx2 Rabbit Model at 1.5 T. *Invest. Radiol.* **2006**, *41*, 410–414.
50. Brown, D. B.; Geschwind, J. F.; Soulen, M. C.; Millward, S. F.; Sacks, D. Society of Interventional Radiology Position Statement on Chemoembolization of Hepatic Malignancies. *J. Vasc. Interventional Radiol.* **2009**, *20*, S317–323.
51. Lo, C-M; Ngan, H.; Tso, W-K; Liu, C-L; Lam, C-M; Poon, RT-P; Fan, S-T; Wong, J. Randomized Controlled Trial of Transarterial Lipiodol Chemoembolization for Unresectable Hepatocellular Carcinoma. *Hepatology* **2002 May 1**, *35*, 1164–1171.
52. Llovet, J. M.; Real, M. I.; Montaña, X.; Planas, R.; Coll, S.; Aponte, J.; Ayuso, C.; Sala, M.; Muchart, J.; Solà, R.; *et al.* Arterial Embolisation or Chemoembolisation *versus* Symptomatic Treatment in Patients with Unresectable Hepatocellular Carcinoma: A Randomised Controlled Trial. *Lancet* **2002**, *359*, 1734–1739.
53. Torchilin, V. Tumor Delivery of Macromolecular Drugs Based on the Epr Effect. *Adv. Drug Delivery Rev.* **2011**, *63*, 131–135.
54. Yu, W. W.; Falkner, J. C.; Yavuz, C. T.; Colvin, V. L. Synthesis of Monodisperse Iron Oxide Nanocrystals by Thermal Decomposition of Iron Carboxylate Salts. *Chem. Commun. (Cambridge).* **2004**, 2306–2307.
55. Duan, H.; Kuang, M.; Wang, X.; Wang, Y.; Mao, H.; Nie, S. Reexamining the Effects of Particle Size and Surface Chemistry on the Magnetic Properties of Iron Oxide

Nanocrystals: New Insights into Spin Disorder and Proton Relaxivity. *J. Phys. Chem. C* **2008**, *112*, 8127–8131.

56. Garin, E.; Denizot, B.; Roux, J.; Noiret, N.; Lepareur, N.; Moreau, M.; Mesba, H.; Laurent, J. F.; Herry, J. Y.; Bourguet, P.; *et al*. Description and Technical Pitfalls of a Hepatoma Model and of Intra-Arterial Injection of Radiolabelled Lipiodol in the Rat. *Lab. Anim.* **2005**, *39*, 314–320.
57. Geschwind, J. F.; Artemov, D.; Abraham, S.; Omdal, D.; Huncharek, M. S.; McGee, C.; Arepally, A.; Lambert, D.; Venbrux, A. C.; Lund, G. B. Chemoembolization of Liver Tumor in a Rabbit Model: Assessment of Tumor Cell Death with Diffusion-Weighted Mr Imaging and Histologic Analysis. *J. Vasc. Interventional Radiol.* **2000**, *11*, 1245–1255.
58. Therasse, P.; Eisenhauer, E. A.; Verweij, J. Recist Revisited: A Review of Validation Studies on Tumour Assessment. *Eur. J. Cancer* **2006**, *42*, 1031–1039.
59. Magill, D.; Mouli, S.; Sandberg, J.; Eifler, A. C.; Belkind, N.; Guo, Y.; Nicolai, J.; Klein, R. A.; Lewandowski, R. J.; Ryu, R. K.; *et al.* Abstract No. 18: The Timing of Electroporation after Delivery of Therapeutic Nanoparticles Affects Drug Uptake in Vx2 Tumors. *J. Vasc. Interventional Radiol.* **2011**, *22*, S11–S12.
60. Gaba, R. C.; Baumgarten, S.; Omene, B. O.; van Breemen, R. B.; Garcia, K. D.; Larson, A. C.; Omary, R. A. Ethiodized Oil Uptake Does Not Predict Doxorubicin Drug Delivery after Chemoembolization in Vx2 Liver Tumors. *J. Vasc. Interventional Radiol.* **2012**, *23*, 265–273.
61. Thompson, S. M.; Callstrom, M. R.; Knudsen, B.; Anderson, J. L.; Carter, R. E.; Grande, J. P.; Roberts, L. R.; Woodrum, D. A. Development and Preliminary Testing of a Translational Model of Hepatocellular Carcinoma for MR Imaging and Interventional Oncologic Investigations. *J. Vasc. Interventional Radiol.* **2012**, *23*, 385–395.
62. Guo, Y.; Klein, R.; Omary, R. A.; Yang, G. Y.; Larson, A. C. Highly Malignant Intra-hepatic Metastatic Hepatocellular Carcinoma in Rats. *Am. J. Transl. Res.* **2010**, *3*, 114–120.
63. Chen, H.; Wang, L.; Yeh, J.; Wu, X.; Cao, Z.; Wang, Y. A.; Zhang, M.; Yang, L.; Mao, H. Reducing Non-specific Binding and Uptake of Nanoparticles and Improving Cell Targeting with an Antifouling Peo-B-Pgammamps Copolymer Coating. *Biomaterials* **2010**, *31*, 5397–5407.